Neuro-Oncology Advances

2(1), 1–12, 2020 | doi:10.1093/noajnl/vdaa119 | Advance Access date 15 September 2020

Preclinical and first-in-human-brain-cancer applications of [^{18}F]poly (ADP-ribose) polymerase inhibitor PET/MR

Robert J. Young[†], Paula Demétrio De Souza França[†], Giacomo Pirovano, Anna F. Piotrowski, Philip J. Nicklin, Christopher C. Riedl, Jazmin Schwartz, Tejus A. Bale, Patrick L. Donabedian, Susanne Kossatz, Eva M. Burnazi, Sheryl Roberts, Serge K. Lyashchenko, Alexandra M. Miller, Nelson S. Moss, Megan Fiasconaro, Zhigang Zhang, Audrey Mauguen, Thomas Reiner[‡], and Mark P. Dunphy[‡]

Department of Radiology, Memorial Sloan Kettering Cancer Center, New York, New York, USA (R.J.Y., P.D.S.F., G.P., P.J.N., C.C.R., P.L.D., S.K., E.M.B., S.R., S.K.L., T.R., M.P.D.); Department of Otorhinolaryngology and Head and Neck Surgery, Federal University of São Paulo, São Paulo, Brazil (P.D.S.F.); Department of Neurology, Memorial Sloan Kettering Cancer Center, New York, New York, USA (A.F.P., A.M.M.); Department of Medical Physics, Memorial Sloan Kettering Cancer Center, New York, New York, USA (J.S.); Department of Pathology, Memorial Sloan Kettering Cancer Center, New York, New York, USA (T.A.B.); Department of Neurosurgery and Brain Metastasis Center, Memorial Sloan Kettering Cancer Center, New York, New York, USA (N.S.M.); Department of Biostatistics and Epidemiology, Memorial Sloan Kettering Cancer Center, New York, New York, USA (M.F., Z.Z., A.M.); The Brain Tumor Center, Memorial Sloan Kettering Cancer Center, New York, New York, USA (R.J.Y., A.F.P., T.A.B., A.M.M., N.S.M.); Weill Cornell Medical College, New York, New York, USA (T.R.); Chemical Biology Program, Memorial Sloan Kettering Cancer Center, New York, New York, USA (J.S., T.R.); Department of Radiology, Weill Cornell Medical College, New York, New York, USA (J.S.)

[†]*These authors contributed equally as co-first authors.*

[‡]*These authors contributed equally as co-senior authors.*

Corresponding Authors: Robert J. Young, MD, Department of Radiology, Memorial Sloan Kettering Cancer Center, 1275 York Avenue, New York, NY 10065, USA (youngr@mskcc.org); Mark P. Dunphy, MD (dunphym@mskcc.org).

Abstract

Background. We report preclinical and first-in-human-brain-cancer data using a targeted poly (ADP-ribose) polymerase 1 (PARP1) binding PET tracer, [^{18}F]PARPi, as a diagnostic tool to differentiate between brain cancers and treatment-related changes.

Methods. We applied a glioma model in p53-deficient nestin/tv-a mice, which were injected with [^{18}F]PARPi and then sacrificed 1 h post-injection for brain examination. We also prospectively enrolled patients with brain cancers to undergo dynamic [^{18}F]PARPi acquisition on a dedicated positron emission tomography/magnetic resonance (PET/MR) scanner. Lesion diagnosis was established by pathology when available or by Response Assessment in Neuro-Oncology (RANO) or RANO-BM response criteria. Resected tissue also underwent PARPi-FL staining and PARP1 immunohistochemistry.

Results. In a preclinical mouse model, we illustrated that [^{18}F]PARPi crossed the blood–brain barrier and specifically bound to PARP1 overexpressed in cancer cell nuclei. In humans, we demonstrated high [^{18}F]PARPi uptake on PET/MR in active brain cancers and low uptake in treatment-related changes independent of blood–brain barrier disruption. Immunohistochemistry results confirmed higher PARP1 expression in cancerous than in noncancerous tissue. Specificity was also corroborated by blocking fluorescent tracer uptake with an excess unlabeled PARP inhibitor in patient cancer biospecimen.

Conclusions. Although larger studies are necessary to confirm and further explore this tracer, we describe the promising performance of [^{18}F]PARPi as a diagnostic tool to evaluate patients with brain cancers and possible treatment-related changes.

Key Points

- [18F]PARPi radiotracer can cross the blood–brain barrier.
- [18F]PARPi uptake corresponded to PARP1 expression in brain cancer.
- [18F]PARPi uptake was high in brain cancers and low in treatment-related lesions.

Importance of the Study

We demonstrate that [18F]PARPi PET/MR can differentiate active brain cancer from treatment-related changes with encouraging results. [18F]PARPi uptake is independent of metabolism, which offers an advantage over [18F]fluorodeoxyglucose, and also independent of blood–brain barrier disruption. Our results suggest that this radiotracer may be a useful diagnostic tool either alone or in conjunction with other advanced imaging techniques to evaluate brain cancer patients with growing indeterminate lesions in order to inform clinical treatment decisions.

Positron emission tomography (PET) scans of the brain are often performed to distinguish cancerous entities from benign entities and from treatment-related changes to brain tissue. [18F]fluorodeoxyglucose (FDG) is the only radiotracer currently approved by the United States Food and Drug Administration (FDA) despite its limited sensitivity and specificity due to the high glucose uptake of normal brain and prominent uptake with postoperative and treatment-related inflammatory changes.[1,2] In Europe, amino acid PET radiotracers, in particular [18F]fluoroethyltyrosine ([18F]FET), are widely available and are preferred for brain cancer imaging, as normal brain tissues demonstrate less uptake of radiotracers than glucose tracers, which improves cancer-to-background contrast.[3] A recent meta-analysis indicated that [18F]FET PET is likely superior to [18F]FDG PET in differentiating between brain cancer progression and treatment-related changes, although with overlapping 95% confidence intervals (CIs).[4] Nevertheless, the limited clinical accuracy of current brain PET tracers clearly indicates the need for new diagnostic agents.

We investigated the potential of [18F] poly (ADP-ribose) polymerase 1 inhibitor ([18F]PARPi) as a useful technique to image brain cancers. A preclinical study including a head-to-head comparison of [18F]FET and [18F]PARPi in a mouse U251 xenograft model demonstrated that [18F]PARPi produced superior cancer visualization and lesion-to-contralateral uptake ratios.[5] Unlike with FDG, cancer detection with [18F]PARPi is not based on metabolic activity, but rather on the presence of the DNA-repair enzyme poly (ADP-ribose) polymerase 1 (PARP1) inside the cancer cell nuclei.[6,7] The PARP family of DNA-repair enzymes is overexpressed in many solid cancers, including brain metastases and high-grade gliomas.[8–10] This overexpression is thought to represent a cellular response to the genomic instability and the frequent cell division occurring in cancer cells.[11]

[18F]PARPi radiotracer is structurally similar to the PARP inhibitor olaparib (AstraZeneca), and its ability to target the PARP1 enzyme in the cell nucleus is maintained because the structural modification on the cyclopropane end of the olaparib scaffold does not perturb target binding.[12] In preclinical work, [18F]PARPi has shown xenograft and orthotopic glioblastoma visualization with 45 times greater uptake in diseased than in healthy mouse brain.[13] [18F]PARPi in intracranial U251 xenograft cancers has also shown 2 times greater uptake than in experimentally induced radiation necrosis.[5]

This pilot study was performed to examine the feasibility of [18F]PARPi imaging in patients with brain cancers and treatment-related changes. We hypothesized that active brain cancers will have high [18F]PARPi uptake due to overexpression of PARP1/2 in cancer cells.

Materials and Methods

Preclinical Radiochemistry

[18F]PARPi was synthesized according to previously described methods.[6,14,15] Preclinical synthesis differs from clinical synthesis in 2 ways: (1) [18F]fluoride was eluted with 2 mL solution of K_{222}/K_2CO_3 (Kryptofix [2.2.2] (4,7,13,16,21,24-hexaoxa-1,10-diazabicyclo [8.8.8] hexacosane (22.5 mg)), 0.02 mL 5M K_2CO_3, and 4% MeCN in H_2O in V_{total} = 5 mL); and (2) [18F]PARPi was isolated by preparatory high-performance liquid chromatography using a flow rate of 3.0 mL/min and isocratic 30% acetonitrile in 0.1% triofluoroacetic acid solution as the mobile phase. Radiochemical purity was more than 98% (t_R = 31 min) and molar activity was 37 000 MBq/μmol (1.0 Ci/μmol).

Animal Work

Brain cancer development was modeled in p53-deficient nestin/tv-a mice (ntv-a/p53$^{fl/fl}$) using a glioma model based on the RCAS/tv-a system.[16,17] All mouse experiments were conducted in compliance with protocols approved

by the Institutional Animal Care and Use Committee of Memorial Sloan Kettering Cancer Center (MSK) and followed the National Institutes of Health guidelines for animal welfare. Mice began showing symptoms around 4–5 weeks post-inoculation. To determine the localization of [18F]PARPi in the brain, we compared its distribution to that of FITC–Dextran (Life Technologies, ThermoFisher Scientific), which does not cross the blood–brain barrier. We co-injected 150–170 μCi of [18F]PARPi and 10 kDa FITC–Dextran via the tail vein in cancer-bearing mice. Animals were sacrificed 1 h post-injection and their brains were extracted, frozen, and sectioned. Coronal cryosections were exposed to a storage phosphor autoradiography plate (Fujifilm, BAS-MS2325) overnight at –20°C for radiotracer localization. Adjacent sections were co-stained with Hoechst-33342 and scanned for FITC/Dextran accumulation using a MIRAX scanner. Images were compared using ImageJ to analyze the distribution of FITC–Dextran and [18F]PARPi in the cancer area.[18]

Clinical Radiochemistry

[18F]PARPi was produced under good manufacturing practice conditions under investigational new drug #139,974. Manufacturing procedures were similar to previously reported procedures[19] and are summarized in Supplementary Material.

Study Design

This prospective, single-center, investigator-initiated pilot study (Clinical Trial NCT04173104) examined [18F]PARPi PET/magnetic resonance (PET/MR) in patients with brain cancers. The primary objective was to determine [18F]PARPi uptake in brain cancers and in treatment-related changes. The study was performed according to the Declaration of Helsinki and Good Clinical Practice guidelines, is compliant with Health Insurance Portability and Accountability Act regulations, and was approved by the MSK Institutional Review Board and Privacy Board. All patients provided written informed consent before enrollment.

Patient Selection

Inclusion criteria were patients harboring new or suspected recurrent brain cancer(s) with enhancing lesion(s) at least 1.5 cm in diameter who were at least 18 years of age and were able to undergo PET/MR scanning and receive intravenous gadolinium contrast. All women of childbearing age had a negative pregnancy test of less than 2 weeks. Exclusion criteria were any contraindication to 3T MRI per departmental criteria. Cohort enrollment was halted at $n = 5$ due to the COVID-19 pandemic, which interrupted all nontherapeutic clinical trials in early 2020.

Patient Imaging

Scans were performed on a 3T PET/MR scanner (Signa, GE Healthcare Systems) with lutetium-based scintillator crystal arrays and silicon photomultiplier detectors integrated into the MR gantry for simultaneous PET and MR acquisition. PET was acquired with intravenous injection of 10 mCi [18F]PARPi and dynamic 60 min acquisition with additional static 10 min acquisitions at 60 min and 120 min. Volumes of interest for standardized uptake value (SUV) measurements were manually placed by a radiologist guided by co-registered MR images, then were internally contoured to select only tracer-avid portions for SUV measurements. SUVs were obtained at 60 min (SUV_{60mean}) and 120 min ($SUV_{120mean}$), as were ratios normalized to the confluence of the cerebral venous sinuses (ratio SUV_{60mean} and ratio $SUV_{120mean}$). MRI was acquired using a 32-channel head coil without and with gadolinium contrast (gadobutrol 0.1 mmol/kg, max 10 mL; Bayer Healthcare) according to standardized brain cancer protocol.[20,21] Per institutional standards, advanced MRI summarized in Supplementary Material was also performed to inform treatment decisions.

Patient Lesion Outcomes

Surgical resection was performed when clinically indicated as per the institutional standard of care. Resected specimens were classified as cancerous when viable cancer tissue was present and as treatment-related changes when no viable cancer tissue was present. If histology was not available due to nonsurgical treatment, lesion outcomes were determined by clinical and imaging follow-up based on Response Assessment in Neuro-Oncology (RANO) criteria for primary brain cancers and RANO brain metastasis (RANO-BM) criteria for secondary brain cancers supplemented by the institutional standard of care advanced imaging.[22–25] In patients with metastases, no more than 5 enhancing lesions at least 1.5 cm in diameter were measured. Per RANO and RANO-BM criteria, respectively, progressive disease was defined as at least 25% increase in the product of perpendicular diameters or at least 20% increase in the sum of longest diameters or clinical worsening; partial response (PR) as at least 50% decrease in the product of perpendicular diameters or at least 30% decrease in the sum of longest diameters; complete response (CR) as disappearance of all enhancing lesions; and stable disease (SD) as all other conditions. PR and CR required sustained effect for at least 1 month.

Blood Time Activity Curves

Blood samples for tracer concentration and metabolite analysis were collected. Blood draws were obtained for 3 patients at 5 time points after the tracer was injected, activity was counted, and metabolites were analyzed (Supplementary Figure 1).

Histopathological Assessment

Lesion outcomes were determined by histopathology when available ($n = 4$). All cases were reviewed by an experienced neuropathologist. The presence of any viable

cancer was considered cancer, and percentages were recorded when possible. One biospecimen included both cancer and treatment-related changes, which were quantified separately.

PARPi-FL Synthesis for Fresh Tissue Staining

PARPi-FL was synthesized using previously described procedures[26] and is summarized in Supplementary Material.

PARP1 Immunohistochemistry

Paraffin-embedded slides were processed at the molecular cytology core facility using previously described protocols,[27] which are summarized in Supplementary Material.

H&E Staining

Paraffin-embedded slides were processed using previously described protocols.[27,28] Slides were scanned (Mirax, 3DHISTECH) to allow for digital histological correlation.

Tabletop Confocal Microscopy

Freshly excised whole-mount patient biospecimens ($n = 4$) were stained with a solution of 100 nM of PARPi-FL in 30% polyethylene glycol in phosphate-buffered saline (PEG/PBS) for 5 min. For the blocking experiment, tissues were co-incubated with 100-fold of olaparib with PARPi-FL. Nuclei were stained with a solution of 10 μg/mL of Hoechst-33342 in PBS. Images were acquired with a laser scanning confocal microscope (LSM880-Live) using 488 nm laser excitation for PARPi-FL (green), 405 nm for Hoechst (blue), and 561 nm (red) for autofluorescence. Quantification of the intensity of PARPi-FL signal was calculated using Fiji (ImageJ)[18] by placing the region of interest on the Hoechst nuclear stain and calculating the signal that emerged in that area using the green channel. Nuclear accumulation of PARPi-FL was calculated using arbitrary units (AUs).

Statistical Analysis

Statistical analysis of the biospecimens was performed using GraphPad Prism 8 (GraphPad Software) and R v3.6.0 (R CoreTeam 2018, R Foundation for Statistical Computing). Data points represent median values, and error bars represent standard deviations. Statistical analyses for the PARP1 expression on immunohistochemistry (IHC) were performed using the Kruskal–Wallis test and correlation with SUV_{max} on 60 min using the Spearman correlation coefficient. Imaging data were examined using the Wilcoxon rank-sum tests. Blocking tissue experiment results were dichotomized at 3 due to the discrete nature of the data and were analyzed using a chi-square test. Statistical significance was determined with $P < .05$ with no correction for multiple testing.

Results

Mouse

[18F]PARPi and FITC–Dextran have nonoverlapping uptake in glioma mouse model

After intracranial diffuse intrinsic pontine glioma (DIPG) were grown in mice ($n = 3$), mice were co-injected intravenously with 150–170 μCi [18F]PARPi and fluorescein isothiocyanate FITC–Dextran (Figure 1A and B). Mice brains were harvested 1 h post-injection, sliced, and imaged. Adjacent slides showed undetectable FITC fluorescence where autoradiography of the adjacent slides presented [18F]PARPi signal (Figure 1C, top and bottom, respectively), suggesting penetration of [18F]PARPi into areas inaccessible to the blood–brain barrier impermeable FITC–Dextran.

Human

Patient distribution

Five patients with 7 enhancing lesions at least 1.5 cm were prospectively enrolled in the study over a 4-month period (December 2019–March 2020), as summarized in Figure 2. Since one patient harbored more than one lesion, we refer to lesion numbers through the paper rather than patient numbers: Patient #1 (lesion #1), patient #2 (lesions #2, #3, and #4), patient #3 (lesion #5), patient #4 (lesion #6), and patient #5 (lesion #7). The median age was 49 years (range 34–56) and 80% of patients were male. Patient data are summarized in Supplementary Table 1; briefly, 3 patients presented with isocitrate dehydrogenase (IDH)-wildtype primary glioblastomas and 2 patients presented with brain metastases (1 with melanoma and 3 lesions, and 1 with renal cell carcinoma). Four lesions (57%) were completely resected after median 2.5 days (range 1–31 days) after PET/MR. Three lesions were histologically confirmed as cancerous, including 1 new untreated glioblastoma and 2 recurrent metastases. Four lesions were treatment-related changes, including 1 after complete resection with no cancer and 3 after standard of care clinical and imaging follow-up.

Patient #1 with glioblastoma was 6 months post 6000 cGy radiation therapy at the time of [18F]PARPi PET/MR. Previous treatments included temozolomide, PARP1/2 inhibitor, combination EGFR variant III, and CD3 immunotherapy; subsequent treatments included bevacizumab, carboplatin, and pembrolizumab. A follow-up to 135 days was consistent with treatment-related changes (SD by modified RANO). Patient #2 had 3 hemorrhagic enhancing lesions that were 19.8, 14.7, and 9.7 months post stereotactic radiosurgery (2100 cGy each). One resected lesion was a recurrent metastasis, and 2 lesions after follow-up were treatment-related changes (both SD by RANO-BM); the patient died from systemic progression 77 days after PET/MR.

High [18F]PARPi uptake on PET/MR correlated with active cancer lesions

[18F]PARPi imaging findings for cancer and treatment-related changes are summarized in Table 1. Despite small

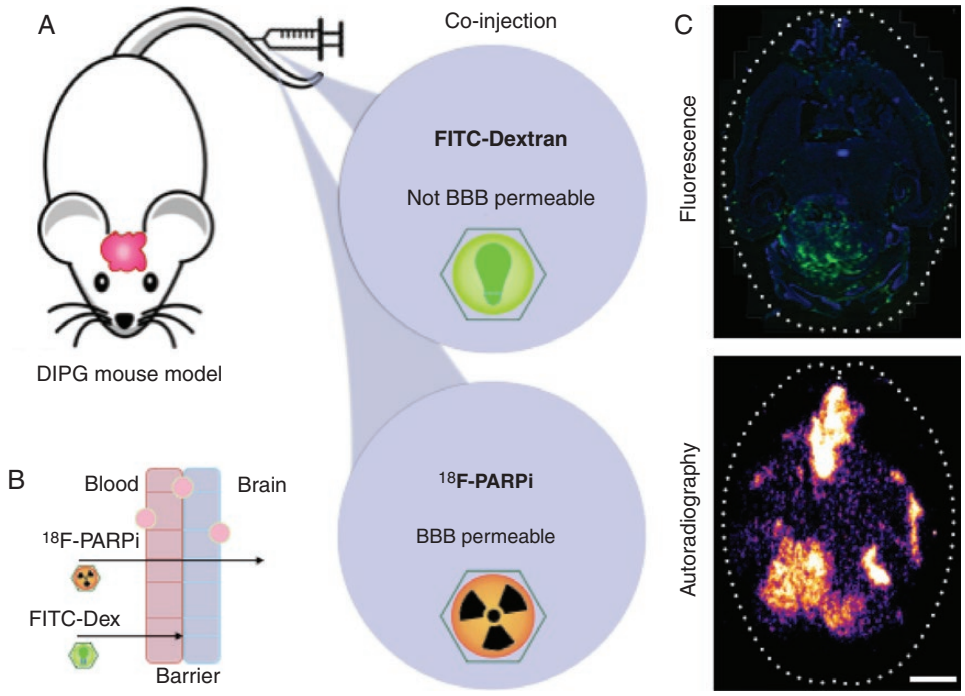

Figure 1. Mouse models demonstrate blood–brain barrier permeability of [18F]PARPi. (A) A DIPG cancer model was grown in mice for 4–5 weeks. Animals were co-injected with 150–170 μCi [18F]PARPi and 10 kDa FITC–Dextran. (B) By analyzing the localization of FITC–Dextran (which does not penetrate the normal blood–brain barrier) and [18F]PARPi post-injection, we demonstrated that an intact blood–brain barrier was able to block dextran passage while allowing [18F]PARPi passage. (C) Mouse brains were harvested 1 h post-injection, sliced, and imaged. Adjacent slides showed undetectable FITC fluorescence where autoradiography of the same slides presented [18F]PARPi signal. Scale bar corresponds to 250 μm.

cohort sizes, the median SUV at 60 min (SUV_{60mean}) and the ratio of lesion-to-normal tissue (ratio SUV_{60mean}) were higher in the cancer group (1.16 and 1.98, respectively) than in the treatment-change group (0.45 and 0.72, respectively; $P = .03$). There was a high correlation between measurements at 60 min and 120 min, with the latter also evidencing an increase in cancers ($P = .03$). In all lesions, the K_{trans} and plasma volume (V_p) perfusion measurements were higher in cancers than in treatment-related changes ($P = .03$). The contrast clearance analysis trended toward higher values in cancers ($P = .08$) than in treatment-related changes. The volume of the enhancing lesion was not different between groups ($P = .70$). Results for individual lesions are reported in Supplementary Table 2.

Lesions with high [18F]PARPi uptake on scans also demonstrated high PARP1 expression in tissue specimens

PARP1 expression of all resected lesions is represented in Figure 3. All 3 resected cancers (lesions #2, #6, and #7) demonstrated high [18F]PARPi uptake at PET and high PARP1 expression in the surgical specimens. The one resected treatment-related change (lesion #5) had low [18F]PARPi uptake on PET and also low PARP1 expression in the surgical specimen.

Tissue specimens were also stained with the fluorescent version of the PARP inhibitor (PARPi-FL) to confirm uptake. Specific nuclear PARPi-FL uptake was seen in all cancers (lesions #2, #6, and #7). Faint PARPi-FL uptake was seen in treatment-related changes (lesion #5; Figure 3A), which was verified to be due to PARP1 expression by submitting the tissues to IHC. Lesion #5 with no viable cancer had a median PARP1 expression over total tissue area of 3% (range 1–5%), which was significantly lower than the expression in all cancer specimens (lesions #2, #6, and #7). Median PARP1 expression over total tissue areas of those lesions were 7% (range 3–14%), 10% (range 7–10%), and 14% (range 11–16%), respectively; $P < .001$; Kruskal–Wallis test (Figure 3B and Supplementary Table 3). The expression strongly correlated with SUV_{max} uptake values measured with [18F]PARPi.

Although the analysis encompasses a small number of data points (only 4 tissue specimens were available), a strong correlation was observed between PARP1 expression and the SUV_{max} at 60 min on the PET scan (Figure 3C). Notably, with few observations for this analysis, lesion #7 was the influential point driving the value.

Intratumoral heterogeneity was demonstrated by different PARP1 expressions

Patient #4 (lesion #6) was scanned with [18F]PARPi at 5.2 months after treatment with laser interstitial thermal therapy. The surgical specimen from this lesion

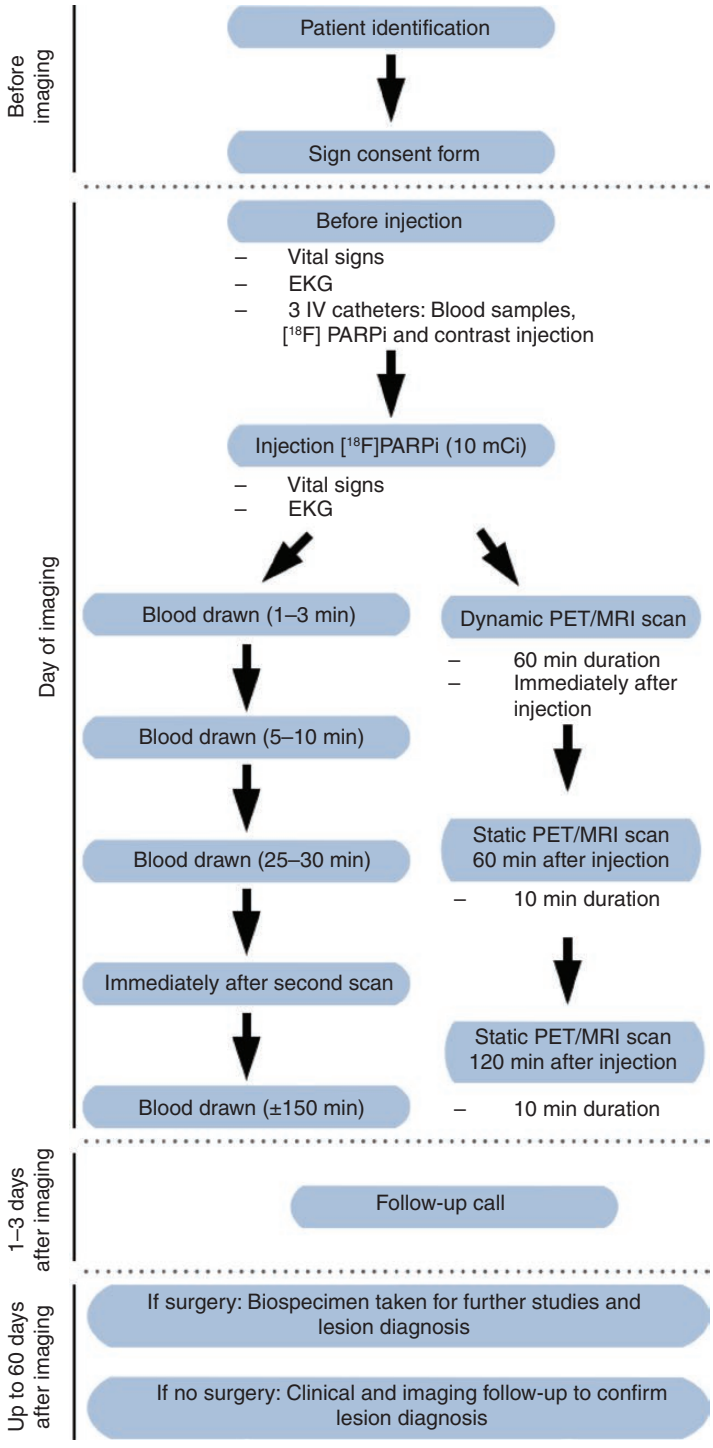

Figure 2. Representation of the study schema. Intervention consisted of 1 PET/MR scan repeated up to 3 times after the injection of 10 mCi [18F] PARPi. Six blood draws (5 mL each) were taken: 5 to access the pharmacokinetics and distribution of the drug and 1 for complete blood count with differential and a complete metabolic panel to access toxicity. Vital signs included temperature, heart rate, blood pressure, and oxygen saturation; none were out of normal range.

consisted of 25% cancer and 75% reactive treatment-related changes with gliosis and histiocytes (Figure 4A). The specimen showed greater PARP1 expression in the area of active cancer than in the area of treatment-related changes, with an average PARP1 expression over total tissue area of 9.33 ± 1.9% versus 0.14 ± 0.06%, respectively (Figure 4B). This patient also presented with areas of high and low [18F]PARPi uptake on the PET/MR

Table 1. Summary of [18F]PARPi Imaging Data

Imaging	Cancer	Treatment-Related Change	*P*
	n = 3[a]	*n* = 4[a]	*Significant
[18F]PARPi SUV_{60mean}	1.16 (1.14–1.19)	0.45 (0.39–0.55)	.03*
[18F]PARPi $SUV_{120mean}$	0.80 (0.76–0.82)	0.34 (0.29–0.45)	.03*
[18F]PARPi ratio SUV_{60mean}	1.98 (1.88–2.00)	0.72 (0.65–0.76)	.03*
[18F]PARPi ratio $SUV_{120mean}$	1.86 (1.69–2.10)	0.95 (0.80–1.05)	.03*
Other advanced imaging			
Enhancing volume (cm^3)	58 (48–66)	80 (42–117)	.7
DCE, rK_{trans}	7.20 (6.10–8.57)	2.21 (1.73–2.58)	.03*
DCE, rV_p	4.28 (3.82–6.16)	1.49 (1.41–1.65)	.03*
Cancer ratio, CCA	0.67 (0.58–0.73)	0.38 (0.36–0.43)	.08

SUV_{60mean}, standardized uptake value 60 min after injection; $SUV_{120mean}$, standardized uptake value 120 min after injection; DCE, dynamic contrast-enhanced T1 perfusion; rK_{trans}, ratio transfer coefficient constant lesion/normal (measure of leakiness); V_P, ratio plasma volume lesion/normal (measure of perfusion); CCA, contrast clearance analysis.
[a]Statistics presented: median (interquartile range, IQR).

similar to the observed differences in PARP1 expression (Figure 4C).

Fluorescent version of the drug confirms specificity

To demonstrate that [18F]PARPi was specific to cancer and not the result of crossing a permeable blood–brain barrier, we stained biospecimens received from surgery with the fluorescent version of the compound (PARPi-FL) and imaged under a fluorescence confocal microscope (Figure 3). Staining and imaging were blinded from the final histopathological result. PARPi-FL uptake was blocked when tissues were co-incubated with 100-fold of olaparib with PARPi-FL (Figure 5A). Quantification of nuclear accumulation was carried out by the presence of PARPi-FL fluorescence signal inside the nucleus of cells. In unblocked tissue (2345 nuclei analyzed), 85% of cells showed PARPi-FL uptake, whereas in blocked tissue (1359 nuclei analyzed), this value was reduced to only 15%. This difference was statistically significant ($P < .001$), confirming blockade of PARPi-FL-specific uptake by saturating the PARP1 enzyme with an excess PARP inhibitor (Figure 5B and Supplementary Table 4).

[18F]PARPi metabolism

Research blood draws were obtained from 3 patients at 5 time points each (1–3 min, 6–7 min, 26–39 min, 91–106 min, and 163 min). Using a 2-phase decay curve, we determined the weighted blood half-life at 1.98 min. At 30 min, and with decreasing blood pool concentration of the injected tracer, we detected a radiometabolite with a retention time of 13.5–16.5 min (58 ± 7%; Supplementary Figure 1A).

[18F]PARPi has lower normal tissue uptake when compared to [18F]FDG

Patient #2 also underwent a PET/CT using the standard of care radiotracer [18F]FDG. Cancer detection with [18F]PARPi is not based on metabolic activity and therefore presented much lower nonspecific uptake in normal brain tissue (Supplementary Figure 2).

Discussion

This study describes the cancer-related localization of [18F]PARPi in mouse glioma models as well as in first-in-human-brain-cancer patients. Increased [18F]PARPi uptake on PET was correlated with increased PARP1 expression in brain cancer biospecimens. Ancillary [18F]PARPi kinetic modeling, PARPi-FL biospecimen imaging, and PARP inhibitor blockade confirmed that the uptake was cancer-specific.

Modern response criteria such as the Response Evaluation Criteria in Solid Tumors (RECIST), RANO, and RANO-BM rely on changes in enhancing size lesions to determine treatment efficacy or failure.[23–25,29] Despite the ubiquity of these and other similar standardized criteria in clinical trials, as well as their growing adoption in clinical practice, there is recognition of the need for advanced imaging techniques to complement these size measurements in treated cancers. After radiation therapy, chemotherapy, and/or immunotherapy, treatment-related changes may occur with growing and/or new enhancing lesions that represent inflammatory-mediated changes rather than worsening cancers. Such treatment-related changes include early pseudoprogression occurring less than 3 months or up to 6–12 months posttreatment, as well as late radiation necrosis occurring many months or years after treatment, which may occur in one-third or more of patients with primary and secondary brain cancers.[30–33]

We investigated a new radiotracer, [18F]PARPi, to bridge this clinical problem. Preclinical research has demonstrated uptake in mouse glioma models which is strongly correlated with PARP1 expression: high in brain cancers (glioma and secondary brain tumors) and low in normal tissues.[5,34,35] Low uptake was seen in experimentally induced radiation necrosis despite blood–brain barrier disruption.[5] Consistent with previous understanding of the mechanism of PARP upregulation in response to DNA damage,[11,12,19,35] we confirmed in humans that increased [18F]PARPi uptake was correlated with active brain cancer and not with treatment-related changes. This has significant implications for patient care, because the accurate and timely noninvasive diagnosis of those changes remains a remarkable imaging challenge. Patients with confirmed recurrent or progressive cancer should stop their current ineffective treatments and instead be considered for possible further resection, radiation therapy,

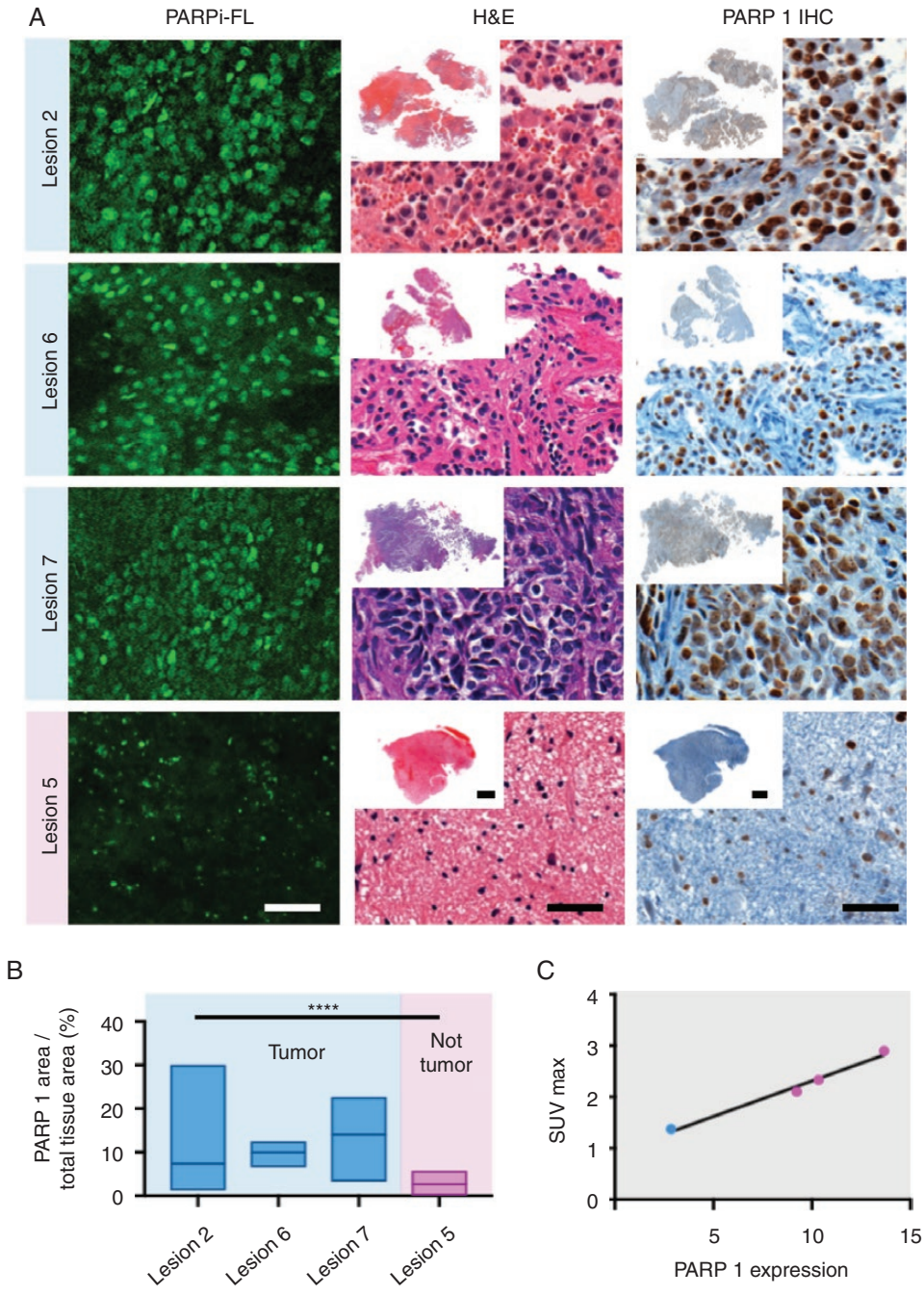

Figure 3. Correlation of PARP1 expression with [18F]PARPi uptake. (A) Specific nuclear PARPi-FL uptake was seen in all cancers (lesions #2, #6, and #7), and faint uptake was seen in treatment-related changes (lesion #5). This differential PARP1 expression was also observed on immunohistochemistry between patients. (B) Differences in quantified PARP1 expression were seen in cancer (blue; lesions #2, #6, and #7) when compared to treatment-related changes (pink; lesion #5). (B) Lesion #5, with no viable cancer, had median PARP1 expression over total tissue area of 3%, which was lower than the expression in all cancer specimens (lesions #2, #6, and #7; 7%, 10%, and 14%, respectively; $P < .001$; Kruskal–Wallis test). (C) Correlation of PARP1 expression and the SUV_{max} of [18F]PARPi at 60 min post-injection. Scale bar in slides with high magnification corresponds to 50 μm and overviews correspond to 0.5 cm.

chemotherapy, and/or immunotherapy, including clinical trials. In contrast, patients with confirmed treatment-related changes should continue their current effective treatment and receive supportive care such as additional steroid therapy rather than embark on more aggressive invasive or investigational therapies. The correlation between [18F]PARPi PET uptake and PARP1 expression confirms its importance in maintaining genome stability and

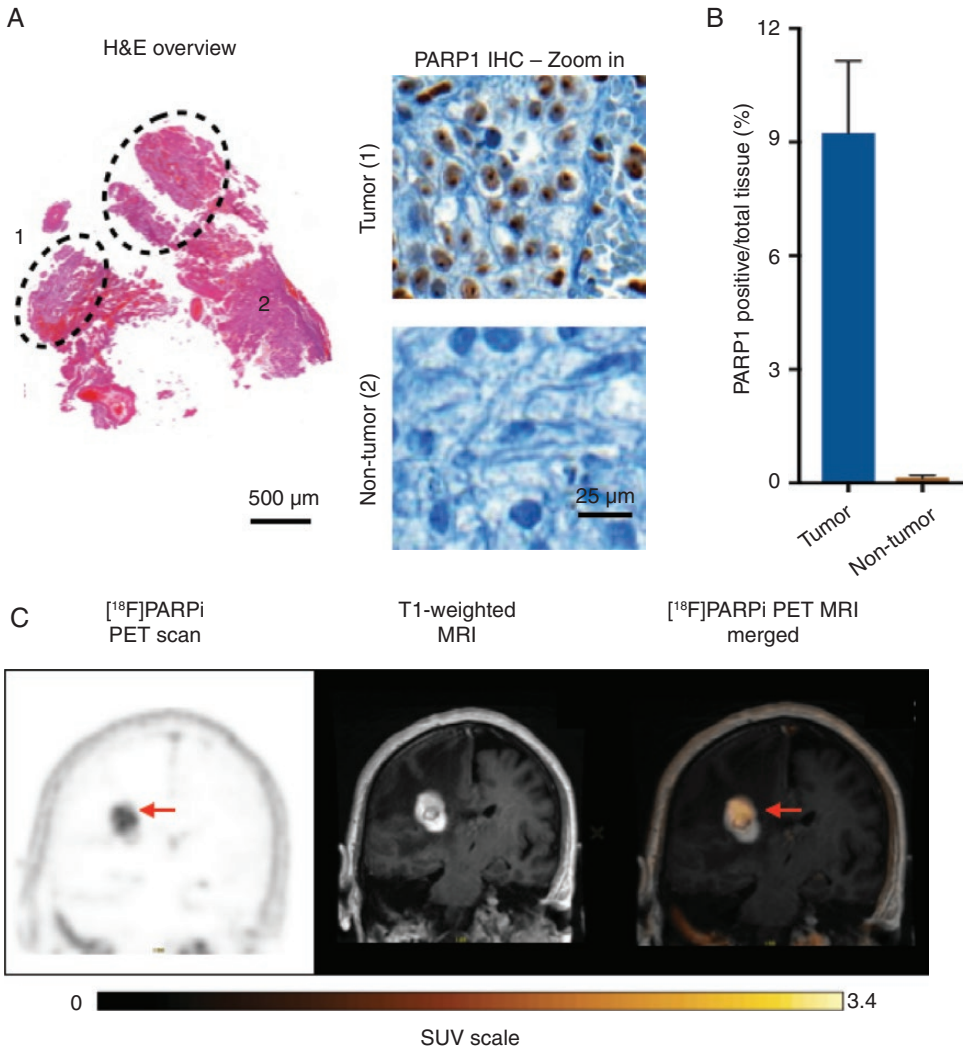

Figure 4. Histology demonstrates [18F]PARPi imaging correlation with PARP1 expression. (A) Lesion #6 biospecimen (metastatic renal cell carcinoma status post-LITT) consisted of a cancer (marked 1 inside the dotted area) and reactive tissue with gliosis and histiocytes (marked 2 outside the dotted area). PARP1 immunohistochemistry showed staining in the cancer areas. (B) Quantification of PARP1 expression over the total tissue area demonstrated that cancer had a substantially higher PARP1 expression than reactive treatment-related changes. (C) Coronal PET/MR images of the parietal lobe taken with [18F]PARPi tracer. Difference in uptake seen on imaging (arrow points to high uptake) is believed to be due to the difference in PARP1 expression seen at histology between areas of cancer and areas of treatment change.

apoptosis in glioblastoma[8] and suggests implications for informing treatment decisions.

[18F]PARPi PET also presents the potential for noninvasive in vivo prediction of drug efficacy. Pretherapy scans already play a role in certain cancers, such as I-123 pretherapy scans in differentiated thyroid cancers before I-131 radioablation.[36] Given specific localization uptake in brain cancers, [18F]PARPi avidity may be useful to quantify PARP1 upregulation in cancer and subsequent sensitivity to systemic PARP inhibitor therapy. This is relevant for brain cancers, as PARP inhibitors are being investigated in several ongoing clinical trials (such as NCT03150862). Additionally, PARP inhibitors are already approved by the FDA for the treatment of solid cancers such as ovarian cancer.[37] PARP inhibitor proof of drug-target engagement has been also demonstrated by PET in preclinical mouse xenograft models of small cell lung and ovarian cancers.[38,39] Demonstrating avid [18F]PARPi PET uptake may provide critical data to identify cancers receptive to subsequent PARP inhibitory therapy versus cancers that may be resistant. Moreover, there are exciting efforts to develop targeted therapeutic options by adding radiotoxic isotopes directly to the olaparib inhibitor scaffold. A recently published study demonstrated promising results using a theragnostic Auger-emitting PARP inhibitor (123I-MAPi) in a preclinical model. Taking advantage of the physical properties of Auger emission, dependent on the proximity of the electron emitter to the DNA to cause cellular damage, along with the biological expression of PARP1/2, which

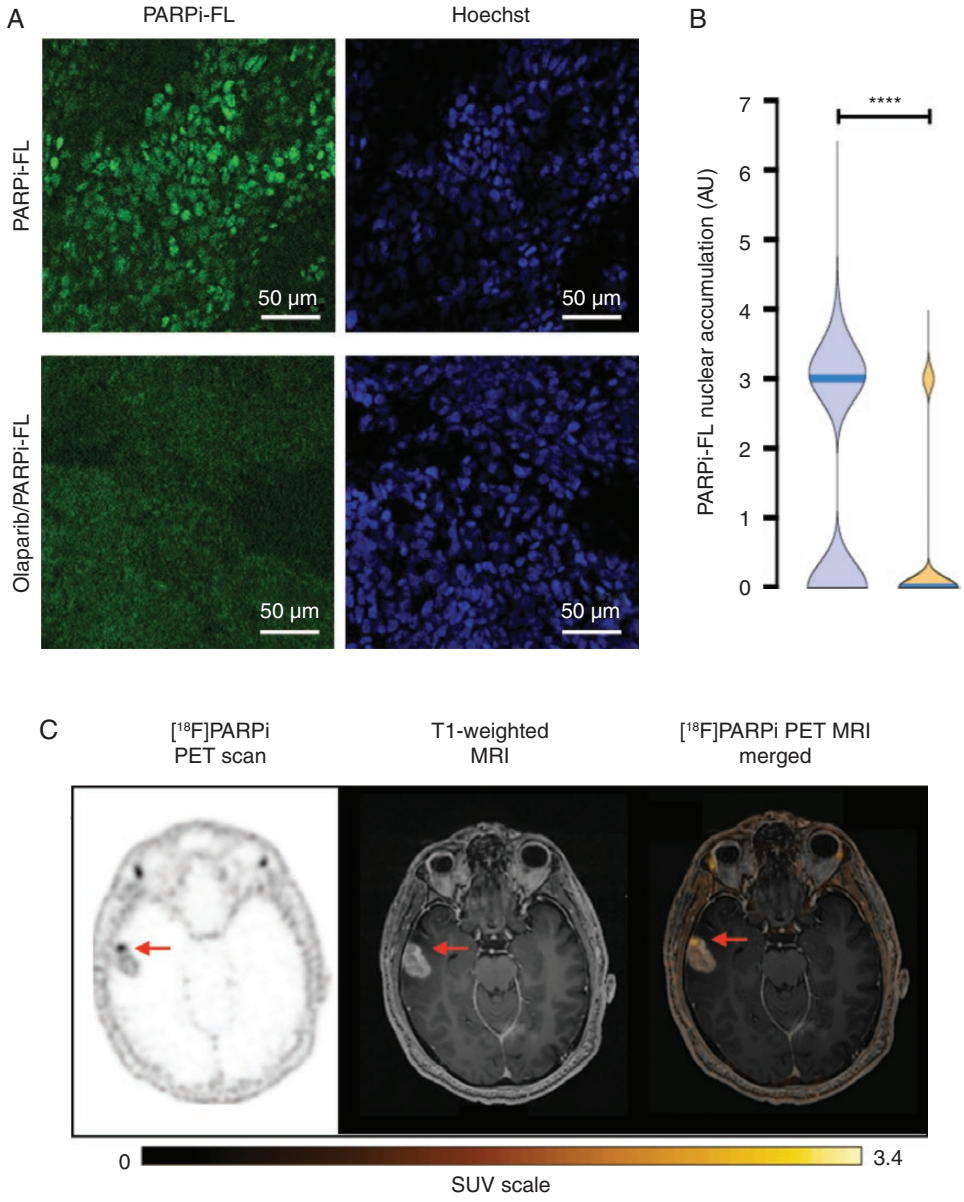

Figure 5. Biospecimen and imaging of lesion #7, untreated glioblastoma. (A) PARPi-FL uptake blocking demonstrates the specificity of the compound. Biospecimen stained with the fluorescent version (PARPi-FL, top row) and blocked (co-incubated with a 100-fold excess of olaparib, bottom row). (B) Quantification of nuclear accumulation of PARPi-FL showed median fluorescence significantly higher ($P < .001$) than in the blocked tissue. (C) Axial [18F]PARPi uptake map, contrast T1-weighted image, and [18F]PARPi map overlaid on contrast T1-weighted image show untreated enhancing cancer in the temporal lobe with high [18F]PARPi uptake (arrow).

is much higher in cancerous than in normal cells, it was possible to achieve lethal cancer doses with limited normal tissue toxicity.[40]

Consistent with the role of PET as an imaging problem-solver, the cancer-specific avidity of [18F]PARPi may also play a role in the differential diagnosis of newly diagnosed brain masses given the apparent lack of correlation with blood–brain barrier disruption that underpins many enhancing brain lesions.[41] The avidity and specificity of the [18F]PARPi tracer in cancer-mimicking conditions, such as tumefactive demyelinating disease, infarction, and abscess, however, are still unknown and warrant further research.

One potential limitation of the study is the small human cohort size. Nevertheless, the results of this prospective, first-in-human-brain-cancer study suggest that [18F]PARPi is safe and that [18F]PARPi PET imaging may successfully discriminate between active brain cancer and treatment-related changes, which is a significant clinical challenge in many patients. A second potential limitation is the absence of histopathology confirmation of cancer versus treatment-related changes in 3 of the 7 lesions included

in the study, for which outcomes were determined by follow-up per standardized response criteria augmented by advanced imaging results. This reflects the realities of clinical care, in which repeat surgery for resection of questionable lesions may not be advisable or feasible in all patients. However, the 4 resected lesions demonstrated excellent correlation between [18F]PARPi uptake and PARP1 expression on IHC, as did the advanced imaging results for all lesions.

In conclusion, we present complementary preclinical data and first-in-human-brain-cancer data demonstrating that [18F]PARPi uptake is specific to cancer and is correlated with PARP1 expression. Although larger trials are necessary, we suggest a role for [18F]PARPi in monitoring patients facing the common clinical dilemma of recurrent or progressive brain cancer versus treatment-related changes, and we anticipate future theragnostic applications for both systemic and combination radiotracer-treatment agents.

Supplementary Data

Supplementary data are available at *Neuro-Oncology Advances* online.

Keywords

brain cancer | [18F]PARPi | PARP1 | PET | PET/MR

Acknowledgments

The authors are grateful for contributions by Matthew Sellitti and the Sloan Advanced Imaging Laboratory (SAIL) and expert editorial advice from Joanne Chin and Alyssa Duck (Department of Radiology, MSK). We also thank Mark Souweidane and Melanie Schweitzer (Department of Neurological Surgery, Weill Cornell Medical College) for helpful discussions and assistance with mouse models. The authors gratefully acknowledge the support of the MSK Animal Imaging Core Facility, MSK Radiochemistry & Molecular Imaging Probes Core, MSK Molecular Cytology Core, MSK Nuclear Magnetic Analytical Core, and MSK Center for Molecular Imaging & Nanotechnology.

Funding

This work was supported by the National Institutes of Health [P30 CA008748, R01 CA204441, R43 CA228815]; Memorial Sloan Kettering Imaging and Radiation Sciences Program; Memorial Sloan Kettering Molecularly Targeted Intraoperative Imaging Fund.

Conflict of interest statement. R.J.Y. has a financial interest in and received funding from Agios Pharmaceuticals and has consulted for Agios Pharmaceuticals, Puma Biotechnology, ICON PLC, and NordicNeuroLab (unrelated to this work). N.S.M. has consulted for AstraZeneca. T.R. and S.K. are shareholders of Summit Biomedical Imaging and co-inventors on filed US patent (WO2016164771) covering use of PARPi-FL and [18F]PARPi. T.R. is co-inventor on US patent (WO2012074840) covering composition of matter for PARPi-FL and [18F]PARPi and is a paid consultant for Theragnostics, Inc. M.P.D., S.K.L., P.D.S.F., G.P., A.F.P., P.J.N., C.C.R., J.S., T.A.B., P.L.D., E.M.B., S.R., A.M., M.F., Z.Z., and A.M. declare no competing interests. All arrangements were reviewed and approved by Memorial Sloan Kettering in accordance with conflict of interest policies. The funding sources were not involved in study design, data collection and analysis, writing of the report, or the decision to submit this article for publication.

Authorship Statement. Conceptualization of study: R.J.Y. and T.R. Establishment of methodology and supervision of procedures: R.J.Y., P.D.S.F., T.R., and M.P.D. Animal experiments and data analysis: P.L.D., G.P., and S.K. PARPi-FL fluorescence and blocking experiments and immunohistochemistry: P.D.S.F. and G.P. Synthesis of PARPi-FL and blood analysis: S.R. Analysis of human tissue specimens: P.D.S.F., G.P., T.R., and T.A.B. Organization and collection of patient data: R.J.Y., M.P.D., A.F.P., and N.M. Assistance with data, including scan investigations: R.J.Y., P.D.S.F., P.J.N., C.R., A.M., N.S.M., and M.P.D. Development of in-house software models: J.S. Provided core and radiopharmaceutical resources: E.M.B., S.R., and S.K.L. Statistical analyses: Z.Z., A.M., and M.F. Writing the original draft: R.J.Y. and P.D.S.F. All authors reviewed, edited, and approved the manuscript.

Data and Materials Availability. All data associated with this study are present in the article or the supplementary materials.

References

1. Furuse M, Nonoguchi N, Yamada K, et al. Radiological diagnosis of brain radiation necrosis after cranial irradiation for brain tumor: a systematic review. *Radiat Oncol*. 2019;14(1):28.
2. Li H, Deng L, Bai HX, et al. Diagnostic accuracy of amino acid and FDG-PET in differentiating brain metastasis recurrence from radionecrosis after radiotherapy: a systematic review and meta-analysis. *AJNR Am J Neuroradiol*. 2018;39(2):280–288.
3. Law I, Albert NL, Arbizu J, et al. Joint EANM/EANO/RANO practice guidelines/SNMMI procedure standards for imaging of gliomas using PET with radiolabelled amino acids and [18F]FDG: version 1.0. *Eur J Nucl Med Mol Imaging*. 2019;46(3):540–557.
4. de Zwart PL, van Dijken BRJ, Holtman GA, et al. Diagnostic accuracy of PET tracers for the differentiation of tumor progression from

treatment-related changes in high-grade glioma: a systematic review and metaanalysis. *J Nucl Med.* 2020;61(4):498–504.
5. Donabedian PL, Kossatz S, Engelbach JA, et al. Discriminating radiation injury from recurrent tumor with [18F]PARPi and amino acid PET in mouse models. *EJNMMI Res.* 2018;8(1):59.
6. Demetrio de Souza Franca P, Roberts S, Kossatz S, et al. Fluorine-18 labeled poly (ADP-ribose) polymerase1 inhibitor as a potential alternative to 2-deoxy-2-[(18)F]fluoro-d-glucose positron emission tomography in oral cancer imaging. *Nucl Med Biol.* 2020;84–85:80–87.
7. Wilson TC, Xavier MA, Knight J, et al. PET imaging of PARP expression using (18)F-olaparib. *J Nucl Med.* 2019;60:504–510.
8. Galia A, Calogero AE, Condorelli R, et al. PARP-1 protein expression in glioblastoma multiforme. *Eur J Histochem.* 2012;56(1):e9.
9. Javle M, Curtin NJ. The role of PARP in DNA repair and its therapeutic exploitation. *Br J Cancer.* 2011;105(8):1114–1122.
10. Curtin NJ, Szabo C. Therapeutic applications of PARP inhibitors: anticancer therapy and beyond. *Mol Aspects Med.* 2013;34(6):1217–1256.
11. Kossatz S, Pirovano G, Demétrio De Souza França P, et al. Validation of the use of a fluorescent PARP1 inhibitor for the detection of oral, oropharyngeal and oesophageal epithelial cancers. *Nat Biomed Eng.* 2020;4(3):272–285.
12. Carney B, Kossatz S, Reiner T. Molecular imaging of PARP. *J Nucl Med.* 2017;58(7):1025–1030.
13. Carney B, Carlucci G, Salinas B, et al. Non-invasive PET imaging of PARP1 expression in glioblastoma models. *Mol Imaging Biol.* 2016;18(3):386–392.
14. Carney B, Kossatz S, Lok BH, et al. Target engagement imaging of PARP inhibitors in small-cell lung cancer. *Nat Commun.* 2018;9(1):176.
15. Tang J, Salloum D, Carney B, et al. Targeted PET imaging strategy to differentiate malignant from inflamed lymph nodes in diffuse large B-cell lymphoma. *Proc Natl Acad Sci U S A.* 2017;114(36):E7441–E7449.
16. Kossatz S, Carney B, Schweitzer M, et al. Biomarker-based PET imaging of diffuse intrinsic pontine glioma in mouse models. *Cancer Res.* 2017;77(8):2112–2123.
17. Becher OJ, Hambardzumyan D, Walker TR, et al. Preclinical evaluation of radiation and perifosine in a genetically and histologically accurate model of brainstem glioma. *Cancer Res.* 2010;70(6):2548–2557.
18. Schneider CA, Rasband WS, Eliceiri KW. NIH Image to ImageJ: 25 years of image analysis. *Nat Methods.* 2012;9(7):671–675.
19. Schöder H, França PDS, Nakajima R, et al. Safety and feasibility of PARP1/2 imaging with 18F-PARPi in patients with head and neck cancer. *Clin Cancer Res.* 2020;26(13):3110–3116.
20. Kaufmann TJ, Smits M, Boxerman J, et al. Consensus recommendations for a standardized brain tumor imaging protocol for clinical trials in brain metastases (BTIP-BM). *Neuro Oncol.* 2020;22(6):757–772.
21. Ellingson BM, Bendszus M, Boxerman J, et al.; Jumpstarting Brain Tumor Drug Development Coalition Imaging Standardization Steering Committee. Consensus recommendations for a standardized Brain Tumor Imaging Protocol in clinical trials. *Neuro Oncol.* 2015;17(9):1188–1198.
22. Zach L, Guez D, Last D, et al. Delayed contrast extravasation MRI: a new paradigm in neuro-oncology. *Neuro Oncol.* 2015;17(3):457–465.
23. Wen PY, Chang SM, Van den Bent MJ, Vogelbaum MA, Macdonald DR, Lee EQ. Response Assessment in Neuro-Oncology clinical trials. *J Clin Oncol.* 2017;35(21):2439–2449.
24. Lin NU, Lee EQ, Aoyama H, et al.; Response Assessment in Neuro-Oncology (RANO) Group. Response assessment criteria for brain metastases: proposal from the RANO group. *Lancet Oncol.* 2015;16(6):e270–e278.
25. Wen PY, Macdonald DR, Reardon DA, et al. Updated response assessment criteria for high-grade gliomas: Response Assessment in Neuro-Oncology working group. *J Clin Oncol.* 2010;28(11):1963–1972.
26. Reiner T, Lacy J, Keliher EJ, et al. Imaging therapeutic PARP inhibition in vivo through bioorthogonally developed companion imaging agents. *Neoplasia.* 2012;14(3):169–177.
27. Kossatz S, Weber WA, Reiner T. Optical imaging of PARP1 in response to radiation in oral squamous cell carcinoma. *PLoS One.* 2016;11(1):e0147752.
28. Kossatz S, Brand C, Gutiontov S, et al. Detection and delineation of oral cancer with a PARP1 targeted optical imaging agent. *Sci Rep.* 2016;6:21371.
29. Eisenhauer EA, Therasse P, Bogaerts J, et al. New response evaluation criteria in solid tumours: revised RECIST guideline (version 1.1). *Eur J Cancer.* 2009;45(2):228–247.
30. Brandsma D, Stalpers L, Taal W, Sminia P, van den Bent MJ. Clinical features, mechanisms, and management of pseudoprogression in malignant gliomas. *Lancet Oncol.* 2008;9(5):453–461.
31. Hatzoglou V, Yang TJ, Omuro A, et al. A prospective trial of dynamic contrast-enhanced MRI perfusion and fluorine-18 FDG PET-CT in differentiating brain tumor progression from radiation injury after cranial irradiation. *Neuro Oncol.* 2016;18(6):873–880.
32. Fink J, Born D, Chamberlain MC. Pseudoprogression: relevance with respect to treatment of high-grade gliomas. *Curr Treat Options Oncol.* 2011;12(3):240–252.
33. Thomas AA, Arevalo-Perez J, Kaley T, et al. Dynamic contrast enhanced T1 MRI perfusion differentiates pseudoprogression from recurrent glioblastoma. *J Neurooncol.* 2015;125(1):183–190.
34. Carlucci G, Carney B, Brand C, et al. Dual-modality optical/PET imaging of PARP1 in glioblastoma. *Mol Imaging Biol.* 2015;17(6):848–855.
35. Salinas B, Irwin CP, Kossatz S, et al. Radioiodinated PARP1 tracers for glioblastoma imaging. *EJNMMI Res.* 2015;5(1):123.
36. Avram AM, Fig LM, Frey KA, Gross MD, Wong KK. Preablation 131-I scans with SPECT/CT in postoperative thyroid cancer patients: what is the impact on staging? *J Clin Endocrinol Metab.* 2013;98(3):1163–1171.
37. Mittica G, Ghisoni E, Giannone G, et al. PARP inhibitors in ovarian cancer. *Recent Pat Anticancer Drug Discov.* 2018;13(4):392–410.
38. Laird J, Lok BH, Carney B, et al. Positron-Emission tomographic imaging of a fluorine 18-radiolabeled poly(ADP-ribose) polymerase 1 inhibitor monitors the therapeutic efficacy of talazoparib in SCLC patient-derived xenografts. *J Thorac Oncol.* 2019;14(10):1743–1752.
39. Makvandi M, Pantel A, Schwartz L, et al. A PET imaging agent for evaluating PARP-1 expression in ovarian cancer. *J Clin Invest.* 2018;128(5):2116–2126.
40. Pirovano G, Jannetti SA, Carter LM, et al. Targeted brain tumor radiotherapy using an auger emitter. *Clin Cancer Res.* 2020;26(12):2871–2881.
41. Sander Effron S, Makvandi M, Lin L, et al. PARP-1 Expression quantified by [18F]fluorthanatrace: a biomarker of response to PARP inhibition adjuvant to radiation therapy. *Cancer Biother Radiopharm.* 2017;32(1):9–15.